Broadband X-ray generation by large krypton clusters under the effect of relativistic femtosecond laser pulses

T.A. Semenov, K.A. Ivanov, A.V. Lazarev, I.N. Tsymbalov, R.V. Volkov, I.A. Zhvaniya, M.S. Dzhidzhoev, A.B. Savel'ev, V.M. Gordienko

Abstract. **This paper presents a phenomenological analysis of thermodynamic parameters of a pulsed supersonic gas jet in a conical nozzle. Conditions have been found out for the condensation and formation of large krypton clusters resulting from phase transitions during adiabatic expansion of gas through the nozzle into vacuum. We have identified the phase state of the large clusters (submicron droplets consisting of $\sim 10^7$ monomers) forming in the jet and obtained a high yield of X-rays from a cluster nanoplasma produced by femtosecond laser pulses of relativistic intensity I. It has been shown that, at $I \approx 3 \times 10^{18}$ W cm^{-2}, a nanoplasma consisting of large krypton clusters emits a broadband X-ray spectrum in the range 5–100 keV. The integrated laser to X-ray energy conversion efficiency achieved is $\sim 10^{-5}$ (400 nJ), and the efficiency of characteristic Kα line (12.6 keV) generation is $\sim 1.5 \times 10^{-6}$ (68 nJ), which corresponds to a quantum yield of $\sim 3 \times 10^8$ photons s^{-1} $(4\pi)^{-1}$, with a contrast of ~ 25 relative to bremsstrahlung background.**

1. Introduction

The development of bright 'table-top' laser-plasma hard X-ray sources (with photon energies $E > 5$ keV) is the subject of intense research [1]. The duration of X-ray pulses from such sources is comparable to that of incident laser pulses ($\sim 10^{-12}$ s), which opens up the possibility of using them as an affordable alternative to radiation from synchrotron facilities and X-ray free-electron lasers (XFELs). Laser-plasma X-ray sources are intermediate in pulse duration between third-generation synchrotron facilities, which have a pulse duration of

T.A. Semenov Faculty of Physics, Lomonosov Moscow State University, Vorob'evy gory, 119991 Moscow, Russia; Institute on Laser and Information Technologies, Russian Academy of Sciences, Svyatoozerskaya ul. 1, 140700 Shatura, Moscow region, Russia; e-mail: physics.letters@yandex.ru;
K.A. Ivanov, A.B. Savel'ev Faculty of Physics, Lomonosov Moscow State University, Vorob'evy gory, 119991 Moscow, Russia; Lebedev Physical Institute, Russian Academy of Sciences, Leninsky prosp. 53, 119991 Moscow, Russia;
A.V. Lazarev Faculty of Chemistry, Lomonosov Moscow State University, Vorob'evy gory, 119991 Moscow, Russia;
I.N. Tsymbalov, R.V. Volkov, I.A. Zhvaniya, M.S. Dzhidzhoev, V.M. Gordienko Faculty of Physics, Lomonosov Moscow State University, Vorob'evy gory, 119991 Moscow, Russia

~ 50 ps, and XFELs, which are capable of ensuring a pulse duration of ~ 10 fs [2]. In characterisation of substances and materials, monitoring of transient intermediates in photochemical reactions [3], investigation of short-lived nuclear isomers [4], and studies of X-ray induced effects in biosystems at a high absorbed dose [5], where use is typically made of synchrotron radiation sources and XFELs, one can apply broadband laser plasma radiation. To date, researchers have demonstrated the possibility of time-resolved X-ray absorption spectroscopy with the use of broadband laser plasma radiation [6]. Moreover, characteristic plasma emission lines are successfully used in time-resolved X-ray structure analysis of matter [2].

The efficiency of hard X-ray generation is determined in large part by the choice of laser targets, which often have the form of condensed media: solids [7], structured targets [8, 9], or liquid jets [6]. A considerable number of laser plasma experiments have been carried out with solid targets in vacuum. Such interaction is typically accompanied by the ejection of target fragments, which result from laser ablation and contaminate the optics and other objects in the chamber. Solid targets limit the number of shots, which depends on the surface area of the targets, usually in the form of moving ribbons, rotating discs, etc. As a result, one has to change them and then adjust the radiation focusing system. A compromise solution is to use microjets of liquid metals, e.g. of gallium [10]. In this approach, however, the problem of vacuum chamber contamination remains unresolved. In the case of liquid jets, one typically has to ensure X-ray generation without vacuum, which reduces the efficiency of the conversion process because ambient air ionisation limits the intensity (clamping) [11].

Cluster jets are an alternative to solid targets in studies of interaction of ultraintense femtosecond laser pulses with matter. A laser-induced relativistic cluster nanoplasma can serve as a source of hard X-rays [12], electrons [13], protons [14], neutrons [15], and terahertz radiation [16]. In addition, it can be used for modelling astrophysical phenomena [17]. Previously reported results [18, 19] demonstrate that a cluster plasma is of interest for obtaining both characteristic and bremsstrahlung X-rays. Efficient X-ray generation is due to the strong laser light absorption in a cluster jet. In particular, even at subrelativistic intensities ($I \sim 10^{17}$ W cm^{-2}) the absorption of the energy of ~ 30-fs laser pulses can reach $\sim 78\%$ [20]. Rapid cluster nanoplasma expansion in a time $t \approx 1$ ps limits the X-ray pulse duration. As a consequence, cluster sources of hard radiation ensure an order of magnitude shorter pulse duration than do solid targets [21]. Cluster jets from nozzle sources combine practical advantages of a gas jet (free from

contaminating solid target fragments and constantly renewable to ensure a high repetition rate) [22] and the strong absorption in a cluster gas medium. Since cluster jet parameters are restored before every interaction event, there is no need to maintain high spatial stability during every laser shot, unlike in the case of solid targets.

Large clusters with a number of monomers above $10^5 - 10^6$ are known to interact effectively with intense subpicosecond laser pulses [23, 24]. With increasing cluster size, the X-ray yield and the degree of ionisation of the forming nanoplasma increase [25]. Cluster nanoplasma heating is mainly caused by a nonlinear resonance absorption [26]. The length scale of cluster heating can be characterised by the free electron oscillation amplitude in the laser field [27], which can be used for evaluating the optimal size of clusters to be used as a laser target. For example, at a laser intensity $I \approx 10^{18}$ W cm^{-2} the optimal cluster size is ~ 100 nm.

Laser – cluster interaction can be optimised by controlling cluster laser target parameters (average cluster size and cluster concentration in the jet), varying the initial temperature and pressure in the nozzle chamber, and adjusting the supersonic nozzle geometry. Note that one concomitant condition with the optimisation of laser – cluster interaction and control over cluster jet parameters is to check whether the cluster jet formation conditions are optimal, which depends in particular on stable operation of the pulse valve. Because of this, the use of optical methods based on test laser light scattering for diagnosing cluster jets is a necessary preliminary step of experiments in question [19].

In the case of Kr clusters, there is considerable interest in experimental studies of the spectrum of highly excited atoms [28] and efficient generation of spectrally bright characteristic X-rays (Kα line, 12.6 keV) [29]. Note also radiation amplification on the ^{26}Kr 3s $\rightarrow$ 2p, transition (~ 1.652 keV) in a filament initiated in a krypton cluster beam by femtosecond laser pulses [30] and electron acceleration in a cluster nanoplasma to MeV energies by relativistic laser pulses [13]. For efficient X-ray generation, use is usually made of targets consisting of high atomic number (Z) elements. In the case of gases, these are Kr and Xe. Note that Kr has the advantage of being readily available.

It is worth noting that X-rays play a key role in the above-mentioned applications, providing information about electron temperature and energy. Interaction of intense femtosecond laser pulses with cluster targets and, hence, nanoplasma generation depend on a number of key parameters, such as the laser pulse intensity, duration, and contrast and the size and concentration of clusters resulting from adiabatic gas expansion into vacuum. Because of this, to reach high efficiency of such X-ray sources it is necessary to optimise cluster jet and laser light parameters.

In this paper, we present a phenomenological analysis of pulsed supersonic krypton cluster jet parameters in a conical nozzle for phase transitions during adiabatic expansion into vacuum. The results make it possible to produce an efficient broadband source of ultrashort X-ray pulses in the range 5 – 100 keV based on large Kr clusters exposed to light from a terawatt peak power femtosecond Ti : sapphire laser system at a relativistic intensity $I \approx 3 \times 10^{18}$ W cm^{-2}.

2. Diagnosis of large cluster formation

In our experiments, Kr cluster jets at initial gas pressures in the range 10 – 60 atm were diagnosed using Rayleigh scatter-

ing measurements. Well-known and easy to implement, this method allows one to monitor clustering in a jet because the scattering signal S_R is related to the cluster concentration (n_{cl}) and the average number of particles per cluster (N_{cl} by $S_R \propto n_{cl} N_{cl}^2$ [31]. Figure 1 shows a schematic of the experimental setup. A 5° half-angle, 24-mm-long conical nozzle with a 0.5-mm throat was connected to a Parker gas pulse valve with an outlet orifice diameter of 0.5 mm. The operation of the valve was controlled by a controller unit. The gas pulse valve was opened for 2 ms. Gas was admitted into a vacuum chamber, which was pumped by a roughing pump at a rate of 14 L s^{-1}. With the gas admission system in operation, the background pressure in the vacuum chamber did not exceed ~ 150 mTorr. As a 445-nm probe light source, we used a 60-mW diode laser, whose beam was focused onto the axis of the cluster gas jet 1 mm from the nozzle exit by an $f = 67$ cm lens. The plane of polarisation of the probe beam was parallel to the cluster jet propagation direction. The Rayleigh scattering signal was measured by a photomultiplier. An image of the scattering region was recorded by a CCD array.
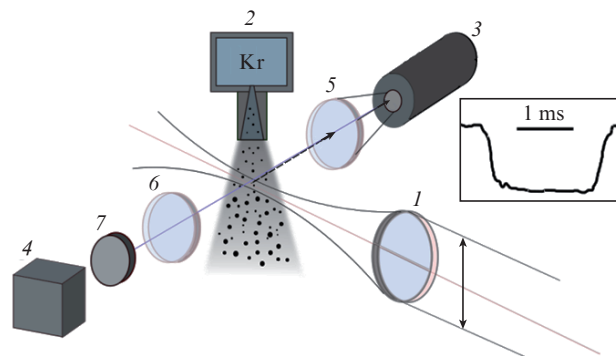

Figure 1. Schematic of the experimental setup for diagnosing cluster jets using Rayleigh scattering:
(1) $f = 67$ cm lens; (2) chamber containing high-pressure gas and connected to a pulsed nozzle; (3) photomultiplier; (4) CCD array; (5) lens; (6) objective; (7) optical filter. The two-headed arrow indicates the polarisation direction of the probe beam. Inset: temporal shape of the scattering signal.
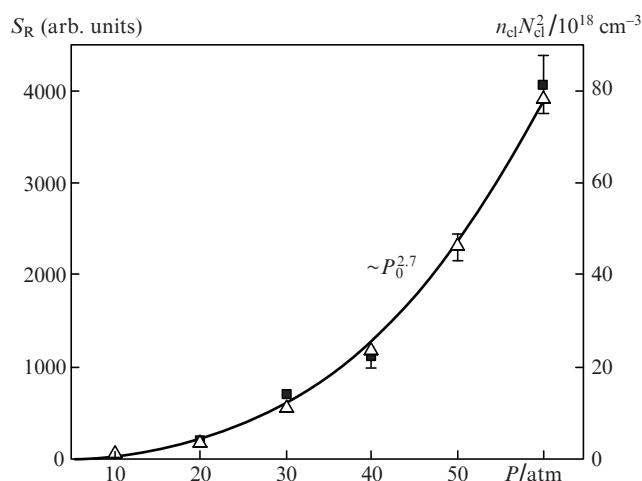
Figure 2. Measured Rayleigh scattering signal as a function of krypton pressure (■) and calculated $n_{cl} N_{cl}^2$ product (△).

As a result, the amplitude of the scattering signal recorded by the photomultiplier was found to be a power-law function of gas pressure [$S_R \sim P^{2.7\pm0.1}$ (Fig. 2)], in agreement with data in the literature [31]. The temporal shape of the scattering signal varied little with gas pressure. A characteristic signal shape is shown in the Fig. 1 inset. The scattering signal profile (Fig. 3) reflects the clustered material density distribution. The cluster jet diameter, measured at a scattering signal to noise ratio of 1.1, is 5 mm. The measured scattering profile of the cluster jet leads us to conclude that the optimal position of the laser focal point is in the highest density zone, which is located about 1 mm from the axis of the conical nozzle.
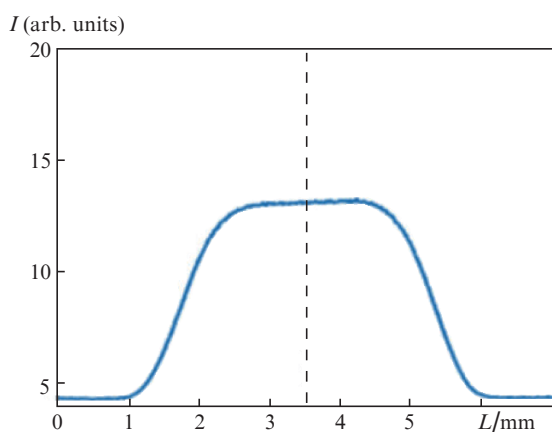

Figure 3. Transverse Rayleigh scattering signal profile at a krypton pressure of 60 atm. The dashed line shows the position of the cluster jet axis.

3. Some aspects of cluster and aggregate formation

At present, there is no consistent description of the formation of large aggregates (clusters, microdroplets, or microcrystals) in gaseous media or jets. The existing phenomenological approaches build on a separate description of clustering [32, 33] and condensation [34] with the use of thermodynamically equilibrium parameters (density, temperature, and pressure) obeying equations of gas dynamics and thermodynamics. It is then convenient to locate regions of clustering and subsequent condensation by analysing the behaviour of expansion isentrops in $P-T$ phase diagrams.

It is known that, during gas expansion in a supersonic jet, only small clusters (no more than ten atoms) are formed before the beginning of the condensation zone because of the highly nonequilibrium state of the system [35]. The formation of aggregates, such as large clusters, microdroplets, and microcrystals, should begin during the gas condensation process. Characteristics of nanoaggregates (size, concentration, and phase state) during gas condensation in supersonic jets depend directly on conditions in the nozzle chamber (pressure P_0 and temperature T_0 determine stagnation conditions) and are controlled by them. In addition, they depend on the nozzle design and the pressure in the gas chamber. Krypton condensation results obtained under the experimental conditions of this study were for the first time described by us based on analysis of the behaviour of expansion isentrops in the relevant $P-T$ phase diagram (Fig. 4). Sublimation (TS), melting
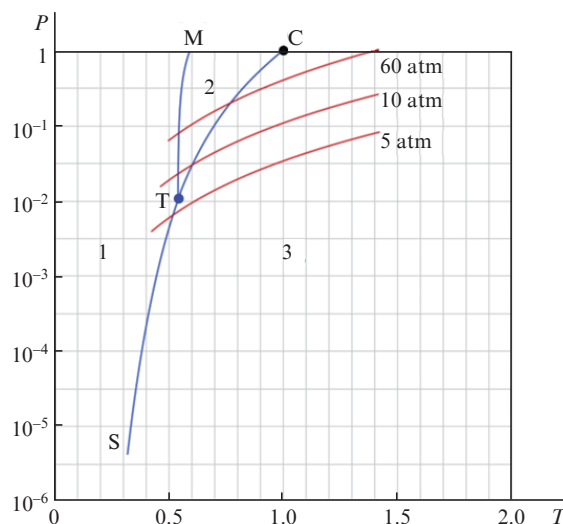
Figure 4. $P-T$ phase diagram of krypton with expansion isentrops (red lines): TC, TM, and TS are the boiling, melting, and sublimation curves; C is the critical point; and T is the triple point. The numbers indicate the (1) solid, (2) liquid, and (3) gas phase fields. The scales of the axes in the $P-T$ phase diagram are normalised to the critical pressure P_{cr} = 54.3 atm and critical temperature T_{cr} = 209.45 K.

(TM), and boiling (TC) curves were obtained using previously reported data [36–38]. The isentrops were calculated using the Redlich–Kwong equation of state [39] with coeficients that ensured calculation accuracy better than 2% in the region of working pressures and temperatures.

During the gas expansion process, the representative point in the $P-T$ phase diagram moves along a 'dry' isentrop (in the absence of condensation) from the initial conditions (P_0 and T_0) to the intersection with a phase equilibrium curve (vaporisation or sublimation curve). In this process, the system remains single-phase (gas). After the intersection with the phase equilibrium curve, the representative point continues to move for some time along the 'dry' isentrop in the condensed phase field (Fig. 4, field 1 or 2), where the system is in a metastable state. The extent of the metastable phase field depends on the time needed to reach a steady-state nucleation rate (time lag), which was variously estimated at between 0.2 and 20 µs [40]. Next, reaching the maximum supersaturation, the system collapses, and the representative point passes to the adiabat of the gas–microdroplet or gas–microcrystal equilibrium two-phase system. The growth of the droplets stops and further increase in particle size is due to the coalescence of small droplets. Finally, the pressure becomes so low that 'quenching' occurs, i.e. the number and size of aggregates remain constant, and only their concentration decreases.

The location of the corresponding zones in and behind the nozzle depends directly on stagnation conditions (P_0 and T_0). With increasing initial pressure P_0 at constant temperature T_0, supersaturation occurs at a higher pressure. Therefore, the zones shift against the flow of the gas jet. In contrast, with increasing temperature T_0 at constant P_0, supersaturation occurs at a lower pressure and the zones shift downstream. The same is caused by the increase in flow velocity upon an increase in the initial temperature T_0. A qualitative analysis suggests that, at the nozzle exit, the jet should contain large krypton aggregates, in the form of microcrystals at a stagnation temperature $T_0 = 298$ K and pressures $P_0 < 7.96$ atm. At

this temperature and higher pressures, the formation of both microcrystals (possibly at $P_0 = 10$ atm) and microdroplets (at $P_0 = 60$ atm) is possible.

Quantitative results can be obtained by solving the corresponding gas dynamics problem, which yields the distribution of flow parameters (density, temperature, and flow velocity) in a particular nozzle and behind its exit. In the case of the conical nozzle used by us, with a slowly varying profile, adequate quantitative estimates can be made using a quasi-one-dimensional model for expansion in a nozzle [41]. This allows the dependence of flow parameters on longitudinal coordinate to be described rather strictly, with cross-sectional averaging. As a result, an independent spatial variable in our case is the coordinate along the nozzle axis, and the cross-sectional area of the nozzle is its function.

It follows from our estimates in the quasi-one-dimensional model for krypton expansion in a 5° half-angle conical nozzle at $P_0 = 5$ atm and $T_0 = 298$ K that condensation begins less than 1 mm downstream from the nozzle throat. Similar results were obtained for argon expansion in a 4° half-angle conical nozzle at $P_0 = 3$ atm and $T_0 = 170$ K in classical nucleation theory [42]. Note that, in the case of conical nozzles, stagnation pressures in the range from 20 to 70 atm, and a temperature of 293 K, the average radius of the krypton condensate (microdroplet or microcrystal) 1.5 mm from the nozzle exit is $55-85$ nm, which corresponds to a number of monomer atoms per cluster from 2.3×10^7 to 8.5×10^7 [43].

Note the following unexpected finding: Despite the above-mentioned separation of the clustering and condensation zones in the jet, the clustering model used by us for describing the krypton aggregation process [33] ensured good agreement of model $n_{cl} N_{cl}^2$ calculations with experimental Rayleigh scattering data (Fig. 2) and calculations using Hagena formulas. At the maximum level of the scattering signal, corresponding to the largest clusters ($P_0 = 60$ atm and $T_0 = 298$ K), calculation using the clustering model yielded an average cluster size $N_{cl} = 5.5 \times 10^6$ (for clusters consisting of monomers) at a cluster concentration in the jet $n_{cl} = 2.6 \times 10^{12}$ cm^{-3}. Calculations using Hagena well-known semiempirical formulas [44] corrected for the case of high pressures give $N_{cl} \approx 6 \times 10^6$ atoms per cluster. With allowance for the Wigner–Seitz radius of Kr ($r_w = 2.15$ Å [45]), the diameter of the clusters under consideration can be estimated at ~ 80 nm. This cluster diameter is comparable to the penetration depth of electrons [27] accelerated by a relativistic laser field of intensity $I \approx 3 \times 10^{18}$ W cm^{-2}, which corresponds to optimal laser heating conditions.

The present results demonstrate that the Weiel model can have a predictive value (cluster concentration and size) in designing experiments aimed at producing targets under supercritical conditions not only in the case of krypton and other inert gases but in the case of molecular compounds, such as CO_2, water, ethanol, and acetone. This will require further experimental verification.

Of special note is that, in identifying supercritical conditions for krypton in the chamber over the nozzle (critical pressure $P_{cr} = 54.3$ atm and temperature $T_{cr} = 209.45$ K), it follows from analysis of the behaviour of isentrops that condensation occurs essentially just behind the nozzle throat, resulting in the formation of a 'large' condensate. With allowance for data reported by Mareev et al. [46] on clustering of carbon dioxide in a similar state, it is reasonable to expect

that critical fluctuations in the high-pressure chamber before expansion will influence the dynamics of clustering during krypton cluster gas jet expansion into vacuum.

Thus, we have performed a phenomenological analysis of supersonic gas jet parameters in a conical nozzle, identified the corresponding phase states, and found out conditions for the formation of large krypton clusters ($d \approx 80$ nm). This allows the present results to be adapted for maximising the yield of X-ray photons from a cluster nanoplasma at a given femtosecond laser output intensity and beam focusing quality.

4. Hard X-ray generation in a relativistic krypton cluster nanoplasma

X-ray emission from a krypton cluster nanoplasma has been studied over the past few decades. Special mention should be given to studies by Zhang et al. [18], Issac et al. [19], and Hayashi et al. [29], which differed drastically in parameters of the experimental setups used and the results obtained. Issac et al. [19] utilised a capillary nozzle at a peak laser power under 2 TW. Such power exceeds the relativistic power of self-focusing, but experimental evidence of such a process in the form of a concomitant filament in Thomson scattering detection is lacking. Zhang et al. [18] carried out their experiments at an intensity of $\sim 3 \times 10^{19}$ W cm^{-2} and an electron density n_e comparable to the critical one, n_{cr}. We call attention to the considerable variation of the effective hot electron temperature from that reported by Issac et al. [19]: 2.9 and 16 keV, respectively.

Hayashi et al. [29] investigated the stability of 12.6-keV characteristic X-rays at a laser beam intensity of 5×10^{16} W cm^{-2}. Based on their results, krypton cluster jets were recommended as a target for use in laser-plasma X-ray sources for radiography. To achieve highly efficient X-ray generation, the ponderomotive energy of plasma electrons should be increased. The use of laser radiation of relativistic intensity allows electrons to gain a ponderomotive energy of hundreds of kiloelectronvolts. Their interaction with a dense nanoplasma ensures efficient bremsstrahlung X-ray generation.

As mentioned above, the results presented in the preceding section on the conditions of the formation of large krypton clusters and their parameters make it possible to optimise the initial conditions for our experimental capabilities. Kr cluster jets were exposed to radiation from a femtosecond Ti : sapphire laser system with a peak output power of 0.9 TW (pulse energy, duration, and repetition rate of 45 mJ, 50 fs, and 10 Hz, respectively). The amplified spontaneous emission (ASE) contrast was $\sim 10^8$ over 100 ps before a main pulse [13].

Figure 5 shows a schematic of the experimental setup. Linearly polarised laser light was focused onto a cluster jet by an off-axis parabolic mirror with $f/D = 6.7$, which ensured a relativistic vacuum laser beam intensity of $\sim 3 \times 10^{18}$ W cm^{-2} (normalised vector potential $a_0 = 1.2$) at a Rayleigh length of 40 μm. Kr clusters were formed as a result of supersonic expansion from a supercritical state of krypton (pressure of 60 atm and temperature of 298 K). The position of the laser focal point was optimised so that eventually it was located in the region of the highest nanoparticle concentration on the front jet boundary 1 mm from the nozzle exit. This was consistent with the Rayleigh scattering intensity profile measured using the CCD array (Fig. 3). In our experiments, we
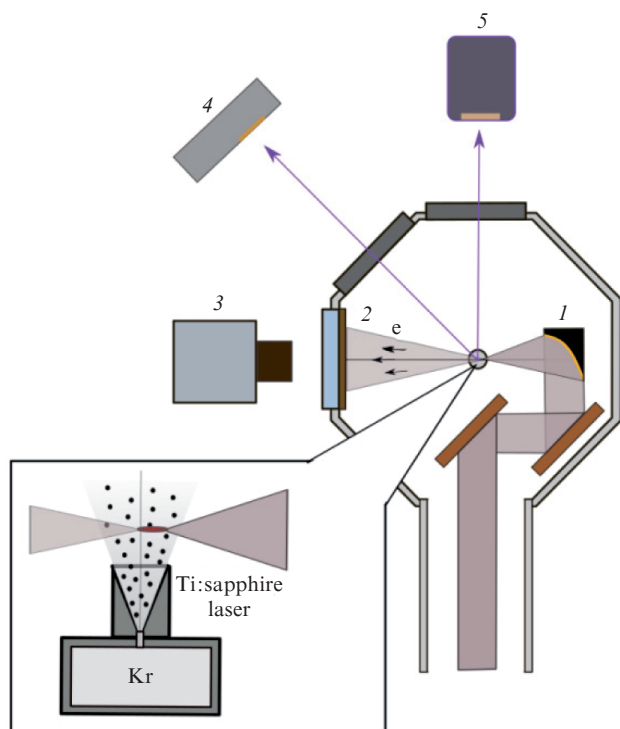
Figure 5. Schematic of the experimental setup for investigation of interaction of femtosecond laser light with a Kr cluster jet:
(*1*) off-axis parabolic mirror with $f/D = 6.7$; (*2*) Lanex scintillator; (*3*) CCD array; (*4*) MediPIX detector; (*5*) Greateyes array.

optimised the gas pressure in the chamber over the pulse valve.

At a krypton pressure of 60 atm, an incident femtosecond laser power of 0.9 TW was found to cause relativistic self-focusing in the cluster jet. That a relativistic intensity was reached and self-focusing developed was ascertained by recording accelerated electron beams on a Kodak Lanex scintillator. The frontside of the Lanex scintillator was protected from optical radiation by 28-μm-thick aluminium foil. According to Monte Carlo simulation of the passage of electrons through aluminium foil with CASINO software [47], an electron beam with an electron energy above 400 keV is transmitted by such filters without distortion. The critical power for relativistic self-focusing was estimated using the well-known formula $p_{\text{las cr}} = 17.4(n_{\text{cr}}/n_{\text{e}})$ GW. Using relations describing supersonic expansion of an ideal gas jet [44], the mean concentration of atoms at the exit of a conical nozzle can be evaluated as $n = 0.01n_0$, where n_0 is the mean concentration of atoms in the high-pressure chamber over the pulse valve of the nozzle. For the highest possible pressure under the conditions of this study, $P = 60$ atm (limitation due to the operation mode of the pulse valve), and normal temperature ($T_0 = 298$ K), we then obtain $n = 1.6 \times 10^{19}$ cm^{-3}. Using data on the degree of ionisation of krypton (+15) at an incident laser beam intensity $I \sim 10^{18}$ W cm^{-2} [48], the mean plasma electron density in the exposed region can be estimated at $n_{\text{e}} \approx 2.4 \times 10^{20}$ cm^{-3} ($n_{\text{cr}} \approx 1.7 \times 10^{21}$ cm^{-3} at a wavelength of 0.8 μm). The critical power for relativistic self-focusing is $p_{\text{las cr}} \approx 0.1$ TW, which is about a factor of 9 lower than the laser output power used.

The evolution of self-focusing was monitored using a lateral image of laser filaments in the cluster jet, obtained with

the CCD array. In recording Thomson scattering, a 0.8-μm interference filter was placed in front of the array. The X-ray spectrum of the nanoplasma was measured using detectors with direct recording of the wanted signal: Greateyes silicon array (5–25 keV) and MediPIX semiconductor detector on a CdTe chip (15–100 keV). Joining the data obtained with the two detectors allowed us to measure for the first time the X-ray spectrum in a wide range: 5–100 keV.

Fine tuning of the position of the laser focal point in the cluster jet was ensured by simultaneously measuring the integrated X-ray yield with the MediPIX detector and monitoring Lanex scintillator glow (Fig. 6). Reaching the optimal X-ray yield was accompanied by electron acceleration to energies above 0.4 MeV. This pointed to a relativistic laser beam intensity in the filament, whose lateral image is presented in Fig. 7. Further increasing the cluster size will cause no increase in generation efficiency because the average cluster size is comparable to the penetration depth of electrons accelerated by a relativistic laser field with an
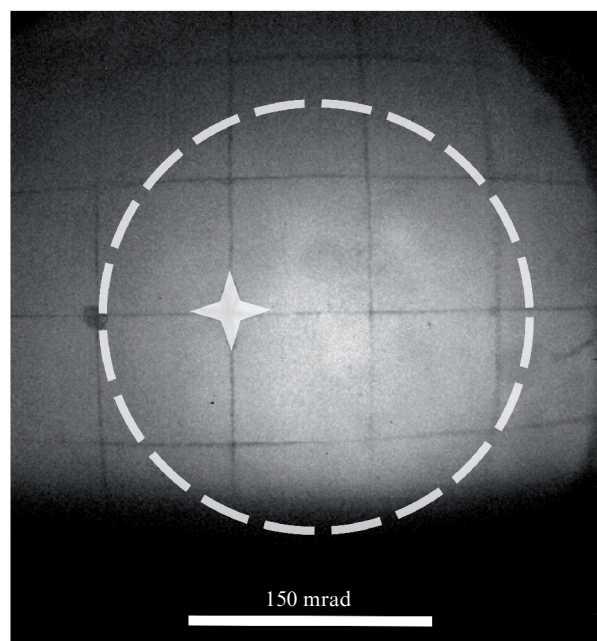

Figure 6. Lanex scintillator glow under the effect of an accelerated electron beam with an ~280-mrad divergence. The asterisk is shown for reference to the recording region.
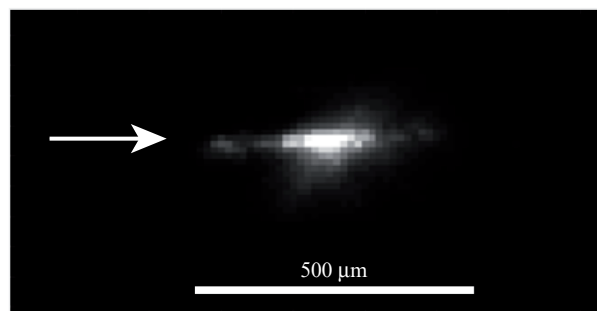
Figure 7. Image of a laser filament in a cluster jet (the arrow indicates the laser light propagation direction).

intensity $I \approx 3 \times 10^{18}$ W cm^{-2}, which corresponds to optimal laser heating conditions.

In our experiments, we recorded the X-ray spectrum of a relativistic krypton nanoplasma in the range 5–100 keV (Fig. 8). The integrated efficiency of laser energy conversion to hard X-rays was $\sim 10^{-5}$ (the total X-ray energy was 400 nJ). In the range 7–35 keV, the spectrum is well fitted by a biexponential function, $A_1 \exp(-E/kT_1) + A_2 \exp(-E/kT_2)$ (where E is the X-ray photon energy), corresponding to a two-temperature electron distribution [19]. The 'temperature' of one electronic component was $T_1 = 1.6 \pm 0.2$ keV and that of the other component was $T_2 = 7 \pm 1$ keV, in agreement with previously reported data [19]. In the energy range 35–100 keV, the X-ray spectrum was well fitted by a function of the form $A_3 \exp(-E/kT_3)$, with an electron 'temperature' $T_3 = 18 \pm 2$ keV. The solid line in Fig. 8 represents the fit to the measured spectrum in the range 7–100 keV. The efficiency of characteristic Kα line (12.6 keV) generation over the full solid angle was found to be 1.5×10^{-6} [or 3×10^8 photons s^{-1} $(4\pi)^{-1}$], in reasonable agreement with data reported by Zhang et al. [18], which were however obtained at an order of magnitude higher laser beam intensity ($\sim 3 \times 10^{19}$ W cm^{-2}) and a power of 20 TW. Measuring the focal spot diameter of the parabolic mirror (4 μm FWHM) and assuming that the pulse duration of the X-ray source is equal to the laser pulse duration (50 fs), we can estimate the peak brightness of the characteristic X-ray (12.6 keV) source made by us. It turns out to be 10^{18} photons s^{-1} mrad^{-2} mm^{-2}, approaching the brightness of third-generation synchrotron sources [2].

Quantum yield/photons $(4\pi)^{-1}$ per pulse
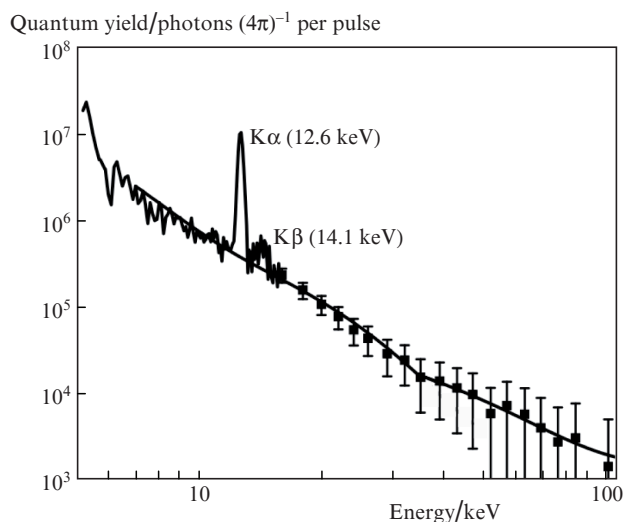
Figure 8. X-ray spectrum of a relativistic krypton nanoplasma. Gas stagnation pressure, 60 atm.

The size of the X-ray source was estimated from the Thomson scattering localisation region, which depends on laser beam intensity and electron density. Therefore, filament regions where the highest plasma density and laser energy are concentrated have the highest radiance. Estimates of the dimensions of the X-ray source showed that its length was 187 ± 70 μm (Fig. 7).

A source of ultrashort hard X-ray pulses in the range 5–100 keV based on a relativistic Kr cluster nanoplasma generated by a terawatt femtosecond Ti:sapphire laser system can be used in a number of applications. In particular, combined with polycapillary optics [49], whose distinctive feature is a broad energy transmission spectrum, such a source will allow X-rays to be focused to a spot diameter of ~ 100 μm. The efficiency of photon focusing onto a sample can reach $\sim 10^{-4}$ of the number of photons emitted by the source over the full solid angle. This estimate was made with allowance for the spectral efficiency of polycapillary optics, $\sim 10\%$, and the characteristic solid angle of X-ray collection from the source, ~ 0.01 sr [49]. Such an X-ray source can be used in applications concerned with analysis of absorption spectra of materials [X-ray absorption near edge structure (XANES) and extended X-ray absorption fine structure (EXAFS)]. An important point is that, unlike sources based on solid targets, laser–cluster X-ray sources are capable of continuously operating for a long time, only limited by the amount of gas in the high-pressure chamber.

5. Conclusions

We have performed a phenomenological analysis of supersonic gas jet parameters in a conical nozzle, identified the corresponding phase state, and found out conditions for the formation of large krypton clusters (droplets ~ 80 nm in diameter) in order to maximise the yield of X-ray photons from a relativistic cluster nanoplasma at a given femtosecond laser output intensity and beam focusing quality.

The X-ray emission spectrum of a relativistic Kr cluster nanoplasma has been measured for the first time in a wide range of X-ray photon energies (5–100 keV) using a repetitively pulsed terawatt femtosecond laser system at an output intensity $I \approx 3 \times 10^{18}$ W cm^{-2}. The spectrum of plasma electrons in this range can be represented as the sum of three exponentials with electron temperatures of 1.6 ± 0.1, 7 ± 1 and 18 ± 2 keV. Direct measurements of the forming electron beam have demonstrated the presence of a considerable number of electrons with energies above 400 keV. The ultrashort hard X-ray pulse source made by us has an integrated laser to X-ray energy conversion efficiency of $\sim 10^{-5}$ (400 nJ). Its length is ~ 200 μm, and the efficiency of characteristic Kα line (12.6 keV) generation is $\sim 1.5 \times 10^{-6}$ (68 nJ), which corresponds to a quantum yield of 3×10^8 photons s^{-1} $(4\pi)^{-1}$, with a contrast of 25 relative to the bremsstrahlung spectrum. The peak brightness of the characteristic X-ray source is estimated at 10^{18} photons s^{-1} mrad^{-2} mm^{-2}.

The laser–cluster hard X-ray emitter can find application for intrinsic light excitation of a nanoplasma of the Kr^{83} isomer, with its first, short-lived, level having an energy of 9.4 keV and its second, long-lived, level at 41.6 keV [50, 51].

Investigation at a krypton pressure of 60 atm in the chamber over the pulse valve involved the formation of nanoaggregates under supercritical initial conditions far from the phase transition to a supercritical state. Recently obtained data on cluster growth in a CO_2 jet resulting from expansion from a supercritical state in the Widom delta [46] suggest that similar behaviour should be expected in the case of Kr cluster jets. Note that increasing the cluster density in a Kr jet will allow the fraction of the absorbed laser energy to be increased and will probably lead to an increase in X-ray generation efficiency. The increase in the fraction of clustered substance in the laser-exposed region with increasing X-ray yield is critical for Kr^{83} photoexcitation.

References

1. Schoenlein R., Elsaesser T., Holldack K., Huang Z., Kapteyn H., Murnane M., Woerner M. *Philos. Trans. R. Soc., A*, **377**, 20180384 (2019).

2. Fetisov G.V. *Phys. Usp.*, **63**, 2 (2020) [*Usp. Fiz. Nauk*, **190**, 1 (2020)].

3. Khakhulin D., Otte F., Biednov M., Bömer C., Choi T.-K., Diez M., Galler A., Jiang Y., Kubicek K., Lima F.A., Rodriguez-Fernandez A., Zalden P., Gawelda W., Bressler C. *Appl. Sci.*, **10**, 995 (2020).

4. Yoshimi A., Hara H., Hiraki T., Kasamatsu Y., Kitao S., Kobayashi Y., Konashi K., Masuda R., Masuda T., Miyamoto Y., Okai K., Okubo S., Ozaki R., Sasao N., Sato O., Seto M., Schumm T., Shigekawa Y., Stellmer S., Suzuki K., Uetake S., Watanabe M., Yamaguchi A., Yasuda Y., Yoda Y., Yoshimura K., Yoshimura M. *Phys. Rev. C*, **97**, 024607 (2018).

5. Montay-Gruel P., Bouchet A., Jaccard M., Patin D., Serduc R., Aim W., Petersson K., Petit B., Bailat C., Bourhis J., Bräuer-Krisch E., Vozenin M.-C. *Radiother. Oncol.*, **129**, 582 (2018).

6. Miaja-Avila L., O'Neil G.C., Uhlig J., Cromer C.L., Dowell M.L., Jimenez R., Hoover A.S., Silverman K.L., Ullom J.N. *Struct. Dyn.*, **2**, 024301 (2015).

7. Zhao T.Z., Batson T., Hou B., Nees J.A., Thomas A.G.R., Krushelnick K. *Appl. Phys. B*, **125**, 8 (2019).

8. Volkov R.V., Gordienko V.M., Dzhidzhoev M.S., Zhukov M.A., Mikheev P.M., Savel'ev A.B., Shashkov A.A. *Quantum Electron.*, **27**, 1081 (1997) [*Kvantovaya Elektron.*, **24**, 1114 (1997)].

9. Ivanov K.A., Shulyapov S.A., Tsymbalov I.N., Akunets A.A., Borisenko N.G., Mordvintsev I.M., Bozh'ev I.V., Volkov R.V., Bochkarev S.G., Bychenkov V.Yu., Savel'ev A.B. *Quantum Electron.*, **50** (2), 169 (2020) [*Kvantovaya Elektron.*, **50** (2), 169 (2020)].

10. Uryupina D.S., Ivanov K.A., Brantov A.V., Savel'ev A.B., Bychenkov V.Yu., Povarnitsyn M.E., Volkov R.V., Tikhonchuk V.T. *Phys. Plasmas*, **19**, 013104 (2012).

11. Garmatina A.A., Bravy B.G., Potemkin F.V., Nazarov M.M., Gordienko V.M. *J. Phys.: Conf. Ser.*, **1692**, 012004 (2020).

12. Kantsyrev V.L., Schultz K.A., Shlyaptseva V.V., Petrov G.M., Safronova A.S., Petkov E.E., Moschella J.J., Shrestha I., Cline W., Wiewior P., Chalyy O. *Phys. Rev. E*, **94**, 053203 (2016).

13. Zhvaniya I.A., Ivanov K.A., Semenov T.A., Dzhidzhoev M.S., Volkov R.V., Tsymbalov I.N., Savel'ev A.B., Gordienko V.M. *Laser Phys. Lett.*, **16**, 115401 (2019).

14. Jinno S., Kanasaki M., Uno M., Matsui R., Uesaka M., Kishimoto Y., Fukuda Y. *Plasma Phys. Controlled Fusion*, **60**, 044021 (2018).

15. Quevedo H.J., Zhang G., Bonasera A., Donovan M., Dyer G., Gaul E., Guardo G.L., Gulino M., La Cognata M., Lattuada D., Palmerini S., Pizzone R.G., Romano S., Smith H., Trippella O., Anzalone A., Spitaleric C., Ditmire T. *Phys. Lett. A*, **382**, 94 (2018).

16. Andreev A.A., Platonov K.Yu. *JETP Lett.*, **112**, 550 (2020) [*Pis'ma Zh. Exp. Teor. Fiz.*, **112**, 9 (2020)].

17. Scott R.H.H., Booth N., Hawkes S.J., Symes D.R., Hooker C., Doyle H.W., Olsson-Robbie S.I., Lowe H.F., Price C.J., Bigourd D., Patankar S., Mecseki K., Gumbrell E.T., Smith R.A. *Phys. Plasmas*, **27**, 033301 (2020).

18. Zhang L., Chen L.-M., Yuan D.-W., Yan W.-C., Wang Z.-H., Liu C., Shen Z.-W., Faenov A., Pikuz T., Skobelev I., Gasilov V., Boldarev A., Mao J.-Y., Li Y.-T., Dong Q.-L., Lu X., Ma J.-L., Wang W.-M., Sheng Z.-M., Zhang J. *Opt. Express*, **19**, 25812 (2011).

19. Issac R.C., Vieux G., Ersfeld B., Brunetti E., Jamison S.P., Gallacher J., Clark D., Jaroszynski D.A. *Phys. Plasmas*, **11**, 3491 (2004).

20. Chen L.M., Park J.J., Hong K.H., Choi I.W., Kim J.L., Zhang J., Nam C.H. *Phys. Plasmas*, **9**, 3595 (2002).

21. Dorchies F., Jourdain N., Lecherbourg L., Renaudin P. *Phys. Rev. E*, **98**, 033212 (2018).

22. Papp D., Polanek R., Lecz Z., Volpe L., Conde A.P., Andreev A.A. *IEEE Trans. Plasma Sci.*, **44**, 10 (2016).

23. Lamour E., Prigent C., Rozet J.P., Vernhet D. *J. Phys.: Conf. Ser.*, **88**, 012035 (2007).

24. Gordienko V.M., Dzhidzhoev M.S., Zhvaniya I.A., Platonenko V.T., Trubnikov D.N., Fedorov D.O. *Eur. Phys. J. D*, **67**, 55 (2013).

25. Boldarev A.S., Gasilov V.A., Faenov A.Ya. *Tech. Phys.*, **49**, 4 (2004).

26. Taguchi T., Antonsen T.M., Milchberg H.M. *Phys. Rev. Lett.*, **92**, 20 (2004).

27. Krainov V.P., Smirnov B.M., Smirnov M.B. *Phys. Usp.*, **50**, 9 (2007) [*Usp. Fiz. Nauk*, **177**, 9 (2007)].

28. Hansen S.B., Fournier K.B., Faenov A.Ya., Magunov A.I., Pikuz T.A., Skobelev I.Yu., Fukuda Y., Akahane Y., Aoyama M., Inoue N., Ueda H., Yamakawa K. *Phys. Rev. E*, **71**, 016408 (2005).

29. Hayashi Y., Fukuda Y., Faenov A.Ya., Kando M., Kawase K., Pikuz T.A., Homma T., Daido H., Bulanov V. *Jpn. J. Appl. Phys.*, **49**, 126401 (2010).

30. Borisov A.B., McCorkindale J.C., Poopalasingam S., Longworth J.W., Rhodes C.K. *J. Phys. B: At. Mol. Opt. Phys.*, **46**, 155601 (2013).

31. Zhvaniya I.A., Dzhidzhoev M.S., Balakin A.V., Kuzechkin N.A., Shkurinov A.P., Gordienko V.M. *Quantum Electron.*, **47**, 1005 (2017) [*Kvantovaya Elektron.*, **47**, 1005 (2017)].

32. Smirnov B.M. *Phys. Scr.*, **50**, 364 (1994).

33. Weiel R. *Z. Phys. D*, **27**, 89 (1993).

34. Boldarev A.S., Gasilov V.A. *Mat. Model.*, **15**, 3 (2003).

35. Wegener P.P., Pouring A.A. *Phys. Fluids*, **7**, 352 (1964).

36. Ferreira A.G.M., Lobo L.Q. *J. Chem. Thermodyn.*, **40**, 1621 (2008).

37. Ferreira A.G.M., Lobo L.Q. *J. Chem. Thermodyn.*, **40**, 618 (2008).

38. Gomez-Nieto M., Thodos G. *AIChE J.*, **23**, 6 (1977).

39. Redlich O., Kwong J.N.S. *Chem. Rev.*, **44**, 1 (1949).

40. Andres R.P. *Homogeneous Nucleation in a Vapor, in Nucleation* (New York: Dekker, 1969) p. 80.

41. Pirumov U.G., Roslyakov G.S. *Gazovaya dinamika sopel* (Gas Dynamics in Nozzles) (Moscow: Nauka, 1990) p. 41.

42. Bondarenko E.A. *Fiz. Nizk. Temp.*, **6**, 3 (1980).

43. Boldarev A.S., Gasilov V.A., Faenov A.Ya. *Zh. Tekh. Fiz.*, **74**, 4 (2004).

44. Dorchies F., Blasco F., Caillaud T., Stevefelt J., Stenz C., Boldarev A.S., Gasilov V.A. *Phys. Rev. A*, **68**, 023201 (2003).
45. Smirnov B.M. *Phys. Usp.*, **43**, 5 (2000) [*Usp. Fiz. Nauk*, **170**, 5 (2000)].
46. Mareev E., Semenov T., Lazarev A., Minaev N., Sviridov A., Potemkin F., Gordienko V. *Molecules*, **25**, 5424 (2020).
47. Drouin D., Couture A.R., Joly D., Tastet X., Aimez V., Gauvin R. *Scanning*, **29**, 92 (2007).
48. Gubbini E., Eichmann U., Kalashnikov M., Sandner W. *Phys. Rev. Lett.*, **94**, 053602 (2005).
49. Bargheer M., Zhavoronkov N., Bruch R., Legall H., Stiel H., Woerner M., Elsaesser T. *Appl. Phys. B*, **80**, 715 (2005).
50. Andreev A.V., Gordienko V.M., Savel'ev A.B. *Quantum Electron.*, **31**, 941 (2001) [*Kvantovaya Elektron.*, **31**, 941 (2001)].
51. Nedorezov V.G., Rykovanov S.G., Savel'ev A.B. *Usp. Fiz. Nauk* (2021, in press).